

The structure of strontium-doped hydroxyapatite: an experimental and theoretical study†

Joice Terra^a, Erico Rodrigues Dourado^a, Jean-Guillaume Eon^b, Donald E. Ellis^{*c}, Gabriela Gonzalez^d and Alexandre Malta Rossi^a

^aCentro Brasileiro de Pesquisas Físicas, Rio de Janeiro, Brazil

^bInstituto de Química, Universidade Federal do Rio de Janeiro, Brazil

^cDepartment of Chemistry and Institute of Catalysis in Energy Processes, Northwestern University, Evanston IL, USA. E-mail: don-ellis@northwestern.edu

^dDepartment of Physics, Depaul University, Chicago IL, USA

Received 19th February 2008, Accepted 11th September 2008

First published on the web 5th November 2008

Tools and Resources

Print this article

 Email a friend

Supplementary information

Advanced features

Find citing articles

GO

First-principles modeling combined with experimental methods were used to study hydroxyapatite in which Sr²⁺ is substituted for Ca²⁺. Detailed analyses of cation–oxygen bond distributions, cation–cation distances, and site 1–oxygen polyhedron twist angles were made in order to provide an atomic-scale interpretation of the observed structural modifications. Density functional theory periodic band-structure calculations indicate that the Ca²⁺ to Sr²⁺ substitution induces strong local distortion on the hydroxyapatite lattice: the nearest neighbor Sr–O bond structures in both cationic sites are comparable to pure SrHA, while Sr induces more distortion at site 2 than site 1. Infrared vibrational spectroscopy (FTIR) and extended X-ray absorption fine structure (EXAFS) analysis suggest increasing lattice disorder and loss of OH with increasing Sr content. Rietveld refinement of synchrotron X-ray diffraction patterns shows a preference for the Ca1 site at Sr concentrations below 1 at.%. The ideal statistical occupancy ratio Sr₂/Sr₁ = 1.5 is achieved for ~5 at.%; for higher Sr concentrations occupation of the Ca2 site is progressively preferred.

1. Introduction

Hydroxyapatite (HA) is one of the main ceramics employed in clinical applications for bone and dental regeneration. It offers excellent biocompatibility and ability to bond to bone tissues. One of its main structural characteristics is its ability to accept a great variety of isomorphous substitutions while retaining the hexagonal space group *P6₃/m*. Divalent cations, such as Zn, Fe, Cu, Mg, Ni, Cr, Mn, Co, Sr, Pb and Cd, and anions such as F⁻, Cl⁻, CO₃²⁻ and VO₄³⁻ may substitute for Ca²⁺, OH⁻ and (PO₄)³⁻ in the HA structure. These substitutions modify its thermal stability, the solubility, and textural properties as well as the surface reactivity. Therefore, the biological response of doped HA, *in vitro* and *in vivo*, is also significantly altered by these substitutions. Recent works^{1–3} have focused upon both structural and chemical modifications of calcium phosphates to enhance bone healing and reconstruction. The positive effects of substitution of Zn and Sr for Ca in small concentration may be contrasted with toxic action due to Pb and Cd substitution, and radioactive ⁹⁰Sr among others.

Numerous studies have been carried out in order to explore the effects of calcium substitution by metals in biological and synthetic HA. Despite the considerable number of *in vitro*^{4–7} and *in vivo* studies involving the use of calcium phosphates doped with strontium,^{8–13} few studies have been conducted on the

structural modifications of HA as well as on the incorporation of the metal. Detailed structural characterization has been made by X-ray diffraction (XRD) in samples prepared at high temperatures by diffusion in the solid state,⁴ and more recently by wet synthesis.⁷ Solid-state diffusion produces a material with an extremely high level of crystallinity and large particle sizes, somewhat different from the bioapatite that constitutes calcified tissues. The latter is produced in biological fluid medium and is formed of some amount of poorly crystalline HA and particles of nanometric dimensions. The Rietveld refinements carried out by Bigi *et al.*^{4,7} indicated a preferential substitution of Sr for the so-called Ca2 site in diffusion-produced samples. Similarly, nanocrystalline samples show a preference for the Ca1 site for Sr concentrations of 3.5 at%, while for concentrations ≥ 6 at.% the Ca2 site is favored. From XRD refinements these authors suggest that the preference for site 2 should be associated to the geometry of the sites, since site Ca2 is formed by stacked oxygen triangles while site Ca1 is formed by columns that run across the *c* axis. Zhu *et al.*¹⁴ studied hydroxyapatite doped with strontium, lead and cadmium which was synthesized by a hydrothermal method. According to the authors, Sr substitution for Ca showed no preference for Ca1 *versus* Ca2 sites for concentrations up to 20 at.%.

In the present work, we have synthesized samples of HA containing 0, 1, 5, 10 and 15 at.% Sr by aqueous methods. The parameters for preparation—synthesis temperature, pH, reagent concentration, addition speed, stirring and stoichiometry—have been adjusted in order to produce samples of a single HA crystalline phase, with crystals of dimensions below 100 nm. The samples were then analyzed by X-ray diffraction generated by synchrotron light. High-quality diffraction patterns allowed refinements to be carried out by means of the Rietveld method, providing information about the unit cell parameters, the crystallite size, atomic positions and relative occupation of Ca1 and Ca2 sites. Additional techniques including X-ray fluorescence, Fourier transform infrared spectroscopy (FTIR) and extended X-ray absorption fine structure (EXAFS) were also used to enhance the XRD results and to characterize the stoichiometry and morphology of the HA crystals as well as the local structure of the strontium sites. In addition, we carried out plane-wave pseudopotential DFT calculations on crystalline Sr-doped HA to investigate its structural modifications.

2. Materials and methods

Sample preparation

The samples of strontium-doped apatite, $\text{Ca}_{(10-x)}\text{Sr}_x(\text{PO}_4)_6(\text{OH})_2$ ($x = 0.1, 0.5, 1$ and 1.5), were synthesized according to the method described by Nounah *et al.*¹⁵ Subsequently we refer to these samples as SrHA-X. Through this method, an aqueous solution containing $\text{Ca}(\text{NO}_3)_2$ and $\text{Sr}(\text{NO}_3)_2$ was added dropwise to a $(\text{NH}_4)_2\text{HPO}_4$ solution at a flow rate of 5 ml min^{-1} and temperature of 90°C . The pH of 10 was maintained by NH_4OH addition. After precipitation, the suspension was kept in digestion for 3 h. The precipitate was then separated by filtration and repeatedly washed with boiling deionized water and dried at 100°C . The dried powder was manually ground and particles of size $< 210 \text{ nm}$ were separated by sieving.

Sample characterization

The concentration of calcium, strontium and phosphorous of the SrHA samples was obtained by X-ray fluorescence using a PW 2400 Sequential (Philips) apparatus. [Table 1](#) shows that the concentration of Sr incorporated into the HA was very close to the nominal value. X-Ray diffraction (XRD) experiments were performed on the SrHA-X samples at the ID15B beamline of the European Synchrotron Radiation Facility (ESRF). The incident X-ray energy was 89.5 keV. Debye rings were collected with a two-dimensional MAR345 image plate with a diameter of 345 mm (2300×2300 pixels). In order to increase the instrumental resolution and the number of reflections, the sample was placed at 1150 and 950 mm relative to the detector. The corresponding *d*-spacing ranges for these two distances were 0.93 to 10 \AA (255 reflections) and 0.78 to 10 \AA (434 reflections) respectively. The Debye rings were integrated and geometrical corrections were applied using the MatLab program.¹⁶ The resulting diffraction patterns, with different instrumental resolutions and *d*-spacing ranges, were simultaneously refined by the Rietveld method¹⁷ using the software FullProf.¹⁸

Table 1 (Ca + Sr)/P and Sr/(Ca + Sr) atomic ratios in SrHA-X obtained from X-ray fluorescence

Sample	(Ca + Sr)/P	Sr/(Ca + Sr)	(Ca + Sr)/P	Sr/(Ca + Sr)
Mol% Sr	Nominal	Nominal	Measured	Measured
0	1.67	—	1.68	—
1	1.67	0.010	1.67	0.011
5	1.67	0.050	1.67	0.058
10	1.67	0.100	1.69	0.112
15	1.67	0.150	1.70	0.169

EXAFS spectra were acquired at the strontium K-edge (16.105 keV) using the facilities of the LNLS storage ring (Campinas, Brazil), operated at the energy of 1.37 GeV with a maximum beam current of 120 mA. Monochromatization of the incident beam was achieved using a double Si(111) crystal. No harmonic rejection method was necessary due to the low energy of the ring. Energy calibration of the beam was done using strontium carbonate as a reference. The spectrum was recorded in transmission mode; data were collected typically out to $k = 12 \text{ \AA}^{-1}$ beyond the absorption edge, at ambient temperature. The intensities of the incident and transmitted beams were monitored by argon-filled ionization chambers. The resultant EXAFS spectrum was analyzed by a standard data reduction procedure using the IFEFFIT code.¹⁹ Structural parameters were obtained from least squares fitting in R-space in the k-range 2–9 Å^{-1} , using theoretical phase and amplitude functions obtained from the FEFF8 program.¹⁹ Standard parameters are reported here with the same name as they are defined in the FEFFIT code.²⁰

Vibrational modes of hydroxyl, phosphate and carbonate groups of the SrHA-X samples were detected by FTIR analysis using a Nicolet Magma 760 spectrophotometer, collecting 32 scans in the range 4000–400 cm^{-1} at a resolution of 4 cm^{-1} .

3. Theoretical methodology

Band-structure calculations have been performed on the basis of spin-restricted DFT theory with the Vienna *ab initio* simulation package VASP, using a periodic supercell model.^{21–23} The projector-augmented wave potential and a plane-wave basis set were employed, using the generalized gradient approximation (PAW-GGA) to describe exchange correlation. The Brillouin zone integration was performed using K-point grids (mesh of up to $4 \times 4 \times 4$) for relaxation of bulk structures and for the calculation of total energy and electronic density of states (DOS). The atomic positions were optimized by conjugate gradient and quasi-Newton algorithms until energy differences less than 0.001 eV per cell were obtained. Gaussian smearing was used for relaxation of ionic coordinates and the tetrahedron integration method was used for DOS calculations. Local densities of states were obtained by projecting the plane-wave functions of the electronic eigenstates onto spherical harmonics within selected atomic spheres.

Crystal structure and cell models

The lattice structure of HA has $P6_3/m$ hexagonal symmetry and as such, lattice parameters $a = b \neq c$, $\alpha = \beta = 90^\circ$ and $\gamma = 120^\circ$. Considering the different positions occupied by calcium and oxygen atoms in the space group $P6_3/m$, its formula per unit cell $\text{Ca}_{10}(\text{PO}_4)_6(\text{OH})_2$ can be rewritten as $\text{Ca}_4\text{Ca}_6(\text{PO}_4)_6(\text{OH})_2$. The phosphate tetrahedra PO_4 form basic structural units, while the coordination around the distinct Ca sites defines the $\text{Ca}_1\text{O}_3\text{O}_2$ metaprism and the distorted $\text{Ca}_2\text{O}_3\text{O}_4(\text{OH})$ polyhedron. Ca2 ions are thus coordinated to hydroxyls; as seen in Fig. 1, they form

triangles centered on, and perpendicular to the c axis. Repetition of this pattern along the c axis gives rise to the OH-channel, where the building unit is formed by two monopyramidal polyhedra, each with a triangular base (labeled as Δ and ∇ in the following) occupied by three Ca2 with one OH at the apex, and twisted by 60° relative to each other. The hydroxyls and Ca1 atoms lie along columns parallel to the c crystalline axis in the ratio of 1 : 2 throughout the crystal. Such OH : Ca1 columns in the hexagonal symmetry lead to a honeycomb structure centered at the OH-columns with vertices alternately composed of O1 and O2 triangles centered on the Ca1-columns (see Fig. 1a). Since Ca2, O1 and O2 ions lie in the same crystallographic plane, as shown in Fig. 1b, the coordination of Ca2 with O1 and O2, which in turn are arranged in equilateral triangles coordinated to Ca1 in a metaprismatic structure, implies that Ca2 is linked to two Ca1 adjacent columns, represented by k and l characters. Such linkage will be identified as Ca2-V in the following. In addition, the honeycomb structure implies that each Ca1 column takes part in three honeycomb edges; *i.e.* each Ca1 column (k) has three adjacent columns, which are represented in Fig. 1a by $l1$, $l2$, $l3$ and henceforth identified as Ca1-Y.

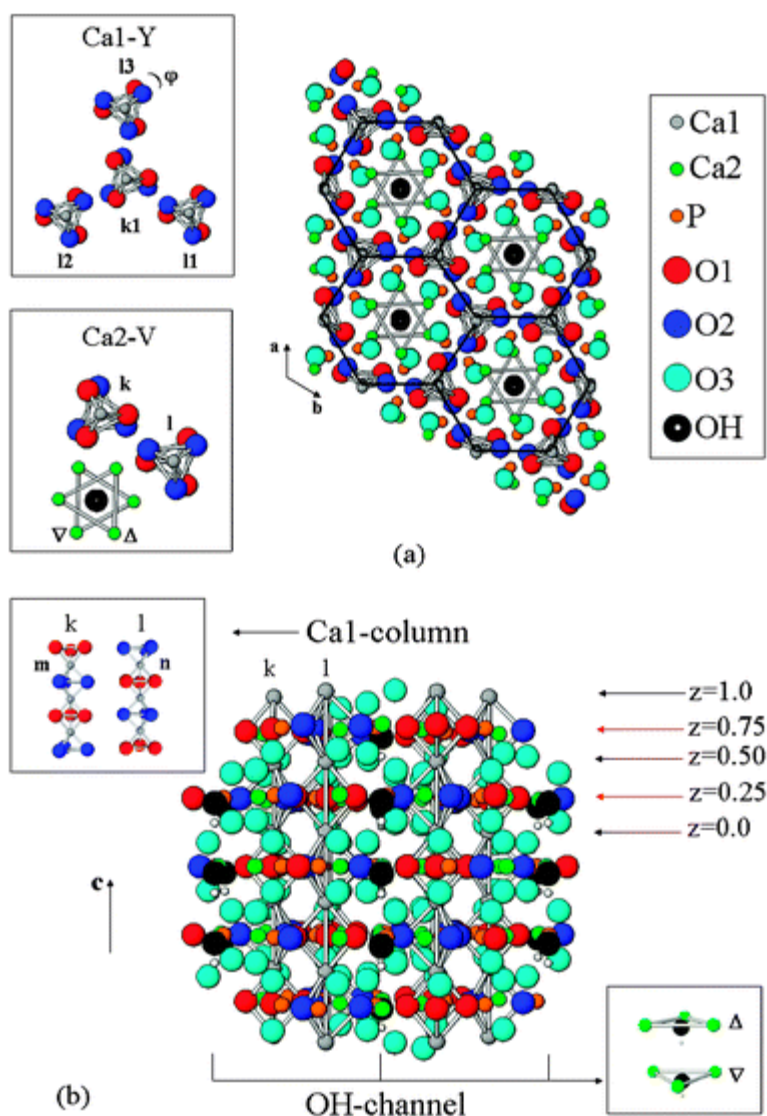


Fig. 1 Calculated pure HA structure: (a) top view; (b) front view. Colored arrows in (b) denote the fractional position along the c direction of Ca1 (in black), Ca2, P, O1, O2 (in red); fractional z positions of O3 and OH are not shown. Amplified views of the Ca1-Y and Ca2-V arrangement as defined in the text, as well as Ca1 adjacent columns (k , l) and Ca2 adjacent triangles (Δ , ∇) are also shown.

A major goal of our theoretical analysis is to determine the Sr energetic preference for non-equivalent Ca1 and Ca2 sites, at different concentrations, and the underlying mechanisms for the preference. The XRD refinements represent *average* cell parameters and site coordinates for a given concentration; theory permits examination at the level of individual sites. To this end, the XRD refinement results were used to construct two species of cells obtained by doubling the HA unit cell along either *a* or *c* directions; namely, $2 \times 1 \times 1$ and $1 \times 1 \times 2$ supercells. The advantage of using two species of cells is that they allow access to different environments around Sr at nonequivalent Ca1 and Ca2 cationic sites. For the sake of brevity, we focus our discussion here entirely upon configurations generated within the $2 \times 1 \times 1$ cell; these data are sufficient to draw general conclusions. Bearing in mind the previous structural discussion, we see that the $2 \times 1 \times 1$ supercells possess four Ca1 columns with two Ca1 ions each or two sets of double Ca1 columns, henceforth named as $\{k1, l1\}$ and $\{k2, l2\}$, and two OH-channels with one $[\Delta, \nabla]$ arrangement of Ca2 in each channel.

The expanded unit cell procedure generates an 88-atom supercell $\text{Ca}_{20-x}\text{Sr}_x(\text{PO}_4)_{12}(\text{OH})_4$, where $x = 0, 1, 2, 3, 4, 20$ actually denotes a 0, 5, 10, 15, 20 and 100 at.% solid solution of Sr in HA. All atomic positions were allowed to relax, while the unit cell parameters were held fixed.

4. Results and discussion

X-Ray diffraction (XRD)

The diffraction patterns of HA samples and those containing 1, 5, 10 and 15 at.% Sr showed typical hydroxyapatite peaks. The Rietveld refinements of XRD \pm patterns confirmed this attribution and revealed no additional mineral phase, see [Fig. 2](#). The unit cell parameters $a = b$ and c increased linearly with the Sr content SrHA-X, as given in [Table 2](#). Cell parameters for 20 at.% Sr used in theoretical analysis have been estimated by a linear fit procedure considering our refinement results and those due to Kay *et al.*²⁴ and Sudarsanan and Young²⁵ for the end members HA ($a = 9.432 \text{ \AA}$, $c = 6.881 \text{ \AA}$) and SrHA-100 ($a = 9.745 \text{ \AA}$, $c = 7.265 \text{ \AA}$) respectively. The resultant equations are: $a = 9.4297 + 0.00531x$ and $c = 6.87689 + 0.00651x$. This behavior indicated that Sr^{2+} , with its larger ionic radius (1.12 vs. 0.99 \AA), effectively substituted for Ca^{2+} in the HA structure. The XRD \pm *average* atomic fractional positions did not present significant variation with respect to pure HA. The Rietveld refinement suggests preferential Sr1 occupation for concentration below 1 at.%, as shown in [Table 3](#). While Sr2 occupancy increases with concentration, it is found to be very close to the statistical value of $\text{Sr2/Sr1} = 1.5$ for 5%. For concentrations of 10 and 15%, Sr2/Sr1 values are 1.80 and 1.98, respectively, showing that site 2 is progressively favored. Sr2/Sr1 values for 10% and 15% are lower than those obtained by Bigi *et al.* for similar Sr concentration. This suggests that Sr occupancy may be sensitive to lattice impurity and preparation methods.^{4,8}

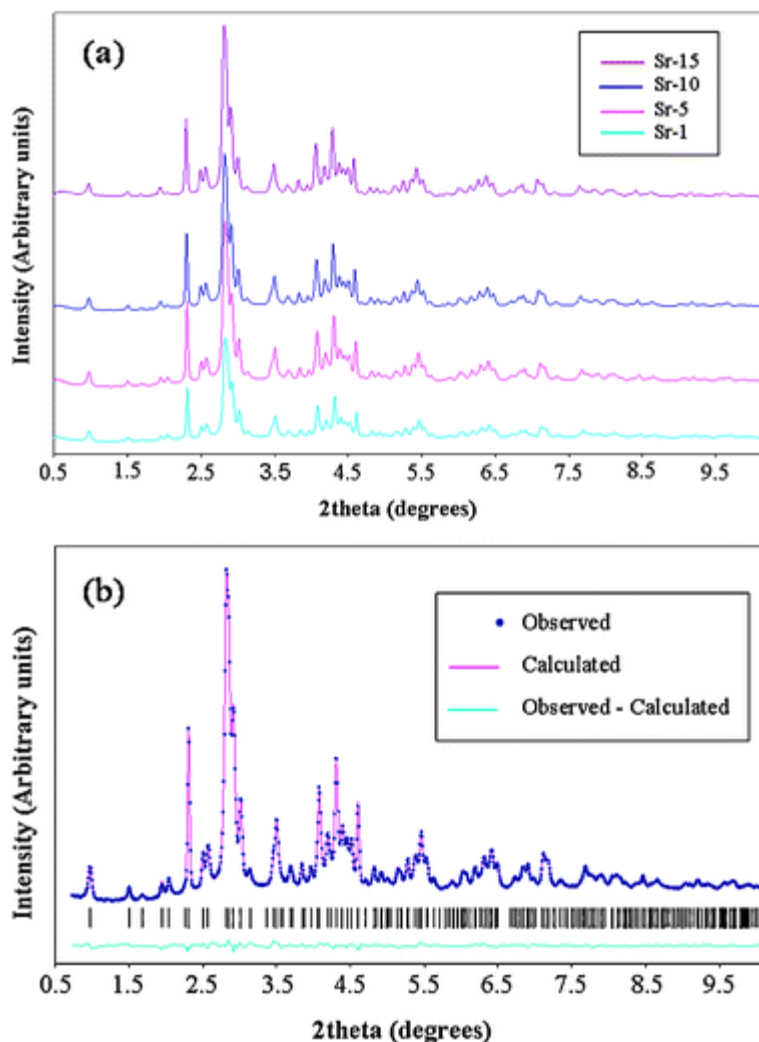


Fig. 2 X-Ray diffraction data. (a) Raw intensities for 1, 5, 10 and 15 at% SrHa-X, (b) Rietveld fit and residuals for 5 at%.

Table 2 Experimental lattice parameters a , c (Å) for Sr content from 1 to 15 at.%. The values for 20% Sr are obtained with a linear fit procedure including HA and SrHA endpoints as described in the text. Error limits are 0.0003 and 0.0002 for a and c respectively

	1%	5%	10%	15%	20%
a	9.4347	9.4520	9.4706	9.4869	9.5062
c	6.8893	6.9041	6.9232	6.9420	6.9609

Table 3 Total atomic occupancy (at.) of Ca and Sr, as well as the Sr1 and Sr2 atomic and fractional (%) occupancies at both sites from Rietveld refinements. Standard deviations are in brackets

Sr (%)	Sr/at.	Ca ₁₀ /at.	Sr1/at.	Sr2/at.	(Sr1/4) × 100 (%)	(Sr2/6) × 100 (%)
1	0.079 (0.043)	9.921	0.074 (0.02)	0.005 (0.02)	1.9	0.1
5	0.431 (0.044)	9.569	0.175 (0.02)	0.256 (0.02)	4.0	4.0

10	0.956 (0.045)	9.044	0.342 (0.02)	0.614 (0.03)	9.0	10.0
15	1.458 (0.051)	8.542	0.490 (0.02)	0.968 (0.03)	12.0	16.0

FTIR

The FTIR spectra of $\text{Ca}_{(10-x)}\text{Sr}_x(\text{PO}_4)_6(\text{OH})_2$ ($x = 0.1, 0.5, 1$ and 1.5) samples are shown in [Fig. 3a–c](#). Sample $x = 0$ presents typical bands of a hydroxyapatite phase.^{26,27} The OH bands ν_L at 633 cm^{-1} and ν_1 at 3571 cm^{-1} decrease in intensity and become broader as Sr is added ([Fig. 3a and b](#)). This suggests that the substitution of Ca by Sr leads to the loss of OH groups and to structural disorder along the c axis. The $\nu_4(\text{PO}_4)$ bands present a slight shift to lower wave numbers and become broader ([Fig. 3a](#)). This also indicates an increase of disorder in the HA structure around phosphate sites as Sr is incorporated. The most intense bands of the HA FTIR spectrum occur within a range of $1150\text{--}950\text{ cm}^{-1}$ and match the vibration modes of the phosphate group at 1092 and 1040 cm^{-1} ([Fig. 3c](#)). These bands do not suffer alteration in position in Sr-doped samples but do become broader as the Sr content rises. These modifications in band linewidth, as shown in [Fig. 3c](#), reinforce the previous suggestion that Sr substitution induces disorder. The broad band observed at 1110 cm^{-1} may be due to a minor fraction of octacalcium phosphate (OCP), $\text{Ca}_8\text{H}_2(\text{PO}_4)_6 \cdot 5\text{H}_2\text{O}$, not detected in XRD, which has a similar structure to HA and is considered one of its precursors. In the $1550\text{--}1350\text{ cm}^{-1}$ range, bands corresponding to carbonate impurities at phosphate sites (B-type) and at hydroxyl sites (A-type) are observed (results not shown). These bands also broaden as Sr is incorporated into HA.

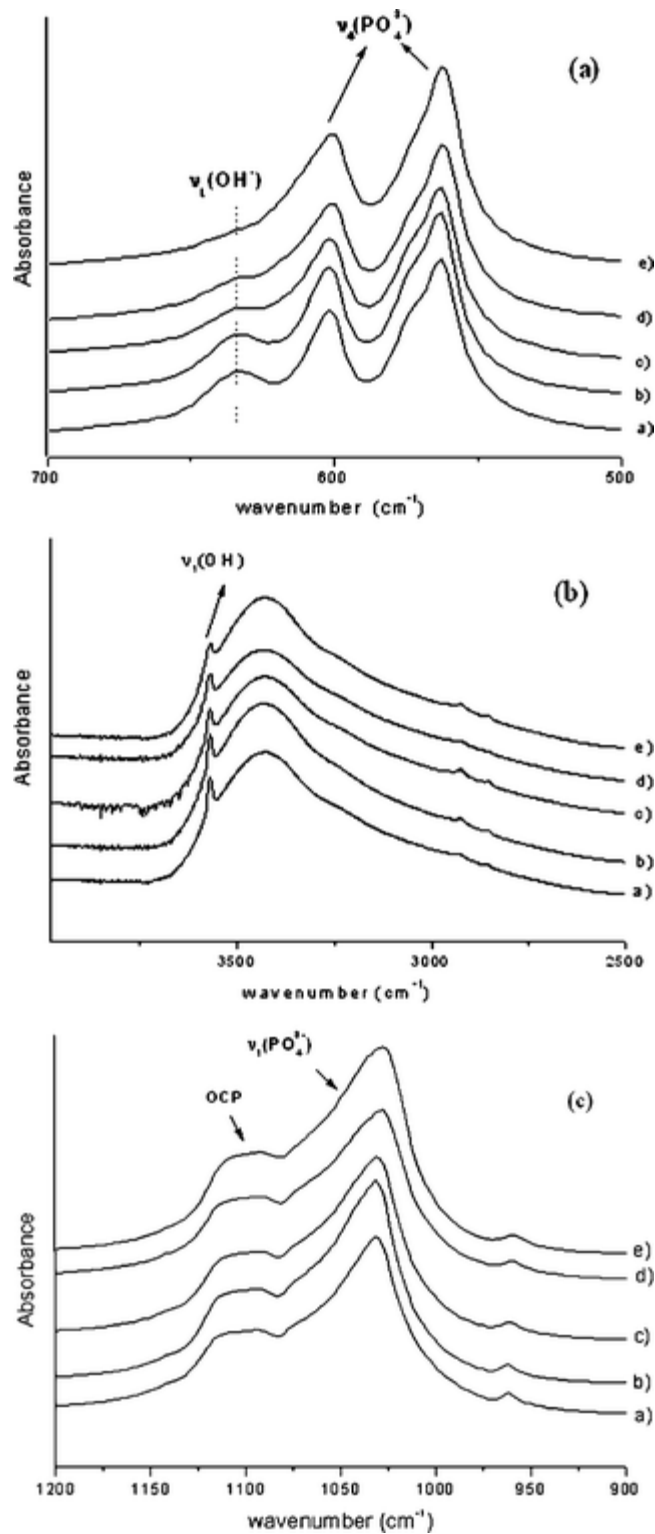


Fig. 3 IR bands of (a) $\nu_1(\text{OH}^-)$ and $\nu_4(\text{PO}_4)$ low frequency regions, (b) $\nu_1(\text{OH})$ high frequency region, (c) $\nu_1(\text{PO}_4)$ region $\sim 1050 \text{ cm}^{-1}$. Curves labeled (a)–(e) represent SrHA-X composition with $x = 0, 1, 5, 10,$ and 15 at.% Sr.

EXAFS

The data and fitting curves for EXAFS of SrHA-15, as precipitated, are shown in [Fig. 4 and 5](#). The Fourier transform (FT) of the EXAFS oscillations, [Fig. 4](#), is quite typical of the hydroxyapatite structure.²⁸ The first

coordination shell was modeled by a single scattering path simulating six oxygen atoms at a single distance of 2.49 Å ($\sigma^2 = 0.008 \text{ \AA}^2$). As discussed below, theoretical values for near-neighbor Sr–O distances range over 2.49–2.61 Å and 2.39–2.68 Å for different configurations of SrHA-X at sites 1 and 2 respectively. Thus the EXAFS distance is compatible with either site. The second feature of the FT spectrum, *i.e.* the doublet in the R -range 3–4 Å, could be very approximately fitted using two single scattering paths associated to 2.3 phosphorus atoms at 3.22 Å and 2.7 phosphorous atoms at 3.65 Å (both with $\sigma^2 = 0.009 \text{ \AA}^2$) and one single scattering path for 8 calcium atoms at 4.09 Å ($\sigma^2 = 0.019 \text{ \AA}^2$). Considering the rather high noise-to-signal ratio, the reported values allowed a fitting of the EXAFS oscillations where the main features of the spectrum are well reproduced, as shown in Fig. 5. The misfit in the magnitude of the FT in the range 3–4 Å is due to differences between the amplitudes of the real and imaginary parts. This is expected; a complete simulation of the spectrum in this range should take into account single scattering paths from oxygen atoms and probably from strontium, as well as some multiple scattering paths.²⁸ The natural disorder associated with the solid solution, and the apparent loss of OH with increasing Sr concentration (see above) is clearly another important factor. The obtained values are nevertheless in excellent agreement with those reported by Harries *et al.*²⁸ and characterize an average distribution of strontium over both crystallographic sites, Ca1 and Ca2, of crystalline HA. It is thus apparent that distances associated to second and third neighbors are not significantly affected by strontium substitution for calcium at low strontium content. This is in contrast with the first coordination sphere which reflects the larger ionic radius of Sr compared to Ca.

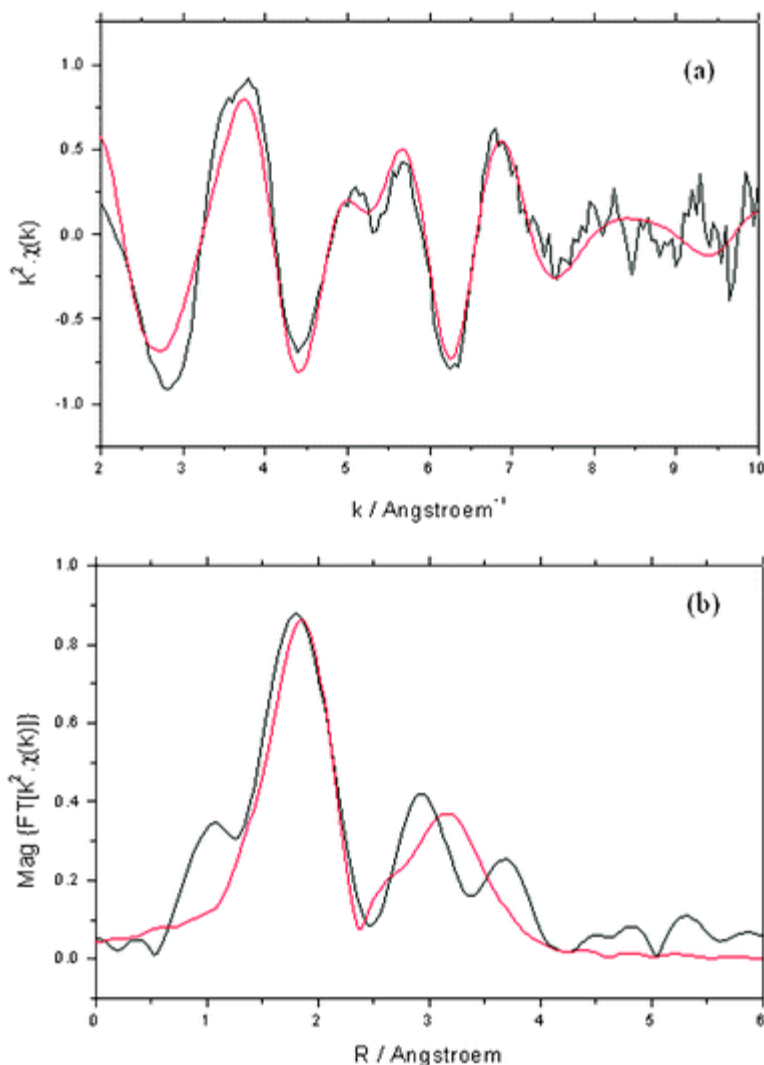


Fig. 4 EXAFS in vicinity of Sr K-edge for SrHA-15. (a) $k^2\chi(k)$ K-space oscillations (black) and fit (red), (b) R -space Fourier transform magnitude (black) and fit (red).

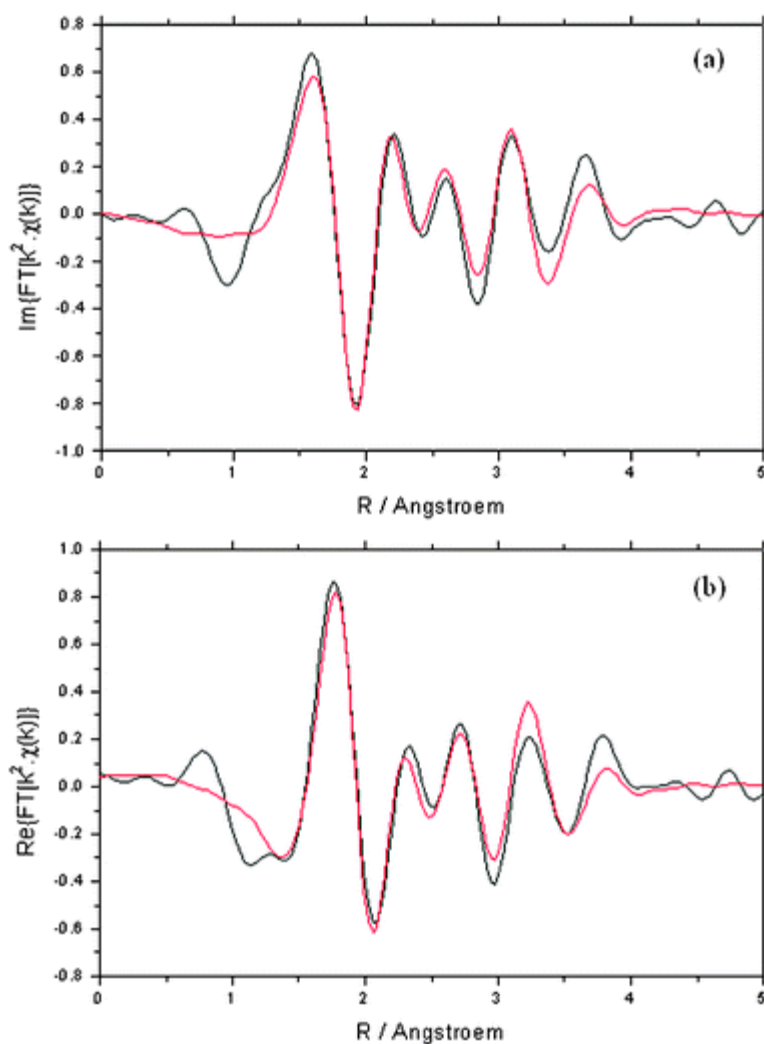


Fig. 5 EXAFS in vicinity of Sr K-edge. (a) Imaginary part of FT, (b) real part of FT.

Periodic DFT calculations

The local densities of states and volume-integrated charges for the various configurations studied are all quite similar. For example, inside a radius R_{WS} of 1.5 Å a typical s, p, d occupancy for Ca is (0.10, 0.14, 0.33) e corresponding to a net charge of +1.44 e ; the net ionicity for Sr (defined somewhat arbitrarily by choice of R_{WS}) is somewhat *greater* than that of Ca. Thus we expect cation–oxygen interactions to be predominantly ionic, as in pure HA. Further details of electronic structure will be presented elsewhere.

Previous discussions of HA structural modifications due to substitution have largely focused on cell-averaged properties which are experimentally accessible, such as average ion radius (connected to the cell parameters) and average twist angles of cation polyhedra. Here we examine fully relaxed *local geometry* of specific cation configurations, to see whether an atomic-level understanding of resulting lattice distortions can be achieved. [Table 4](#) shows the configurations sampled in 211 supercells for compositions of 5, 10, 15 and 20 at.% Sr in the HA structure as well as the corresponding calculated excess energies. The second column in the Table crudely represents the substituted sites: thus, the first cell listed, identified as ‘1’, was obtained by replacing one Ca1 by Sr; similarly ‘2’ denotes substitution at a single Ca2 site, ‘12’ denotes simultaneous substitution at both Ca1 and Ca2, *etc.* As described above, the notation $\{k1(m), l1(n)\} \{k2(m), l2(n)\}$ represents the Sr occupancy at k, l Ca1 columns, where m and n are the number of Ca1 intervening between successive Sr. Then, $k1, l1, k2, l2$ labels supply information about Sr1 occupancy along the a direction, while m and n detail the Sr1 distribution on

planes along the c direction. Further information is also provided with the SP (same plane) and DP (different plane) labels distinguishing multiple Sr insertions. This detailed notation supplies a concise description of varied Sr distributions within the HA structure so that the excess energy values associated with each may be analyzed in terms of local cation–cation interactions and lattice distortions.

Table 4 Calculated excess energies E_x (meV per cation site) versus Sr composition (%) and configuration at Ca sites 1 and 2. The Sr occupancy notation is defined in the text

Composition	Sr site occupancy	Configuration at site 1		Configuration at site 2		E_x
		$\{k1(m), l1(n)\}$	$\{k2(m), l2(n)\}$	$[\Delta, \nabla]$	$[\Delta, \nabla]$	
5	1	$\{1(1), 0(2)\}$	{Ca1}	—		3.4
	2	—		[1,0]	[Ca2]	6.6
10	11	$\{1(1), 1(1)\}$:SP	{Ca1}	—		2.6
	12	$\{1(1), 0(2)\}$	{Ca1}	[1,0]	[Ca2]	9.7
	22	—		[1,0]	[1,0]	13.2
15	111	$\{1(1), 2(0)\}$:SP	{Ca1}	—		10.0
	112	$\{2(0), 0(2)\}$	{Ca1}	[1,0]	[Ca2]	14.5
	122	$\{1(1), 0(2)\}$	{Ca1}	[1,0]	[1,0]	16.1
	222	—		[1,0]	[2,0]	20.8
20	1111	$\{2(0), 2(0)\}$	{Ca1}	—		11.7
	1111a	$\{1(1), 1(1)\}$:DP	$\{1(1), 1(1)\}$:DP	—		12.0
	1222	$\{1(1), 0(2)\}$	{Ca1}	[2,0]	[0,1]	21.4
	2222	—		[1,1]- <i>cis</i>	[1,1]- <i>cis</i>	22.8
	2222a	—		[2,2]- <i>trans</i>	[Ca2]	23.7

As an example of Sr–Sr interaction, consider the ‘11’ cell defined in [Table 4](#), identified by $\{1(1), 1(1)\}$:SP {Ca1}, meaning that two Sr1 ions are placed in adjacent $k1, l1$ columns. Moreover, they are distributed according to the sequence SrCaSrCa..., and they lie in the same Ca1 plane. The other column set $\{k2, l2\}$ has no Sr occupancy and is represented merely as {Ca1}. As a second example, recall that the notation $[\Delta, \nabla]$ is used to identify Sr2 occupancy on one triangle and its adjacent partner along the c -axis (see [Fig. 1b](#)). A further index is needed to classify the orientation of multiple Sr2 sites on one triangle relative to another (-*cis* vs. -*trans* occupancy, see the OH-channel inset of [Fig. 1](#)). Thus, consider the configuration listed as ‘22’ in [Table 4](#), identified as [1, 0] [1, 0], specifying that both Sr are positioned at Ca2 triangles with identical orientation, however, belonging to different channels. For a 211 supercell, we note that all OH-channels present Sr2 substitution and the occupancy sequence along the c direction is given by $\{\Delta\text{-Sr } \nabla\text{-Ca } \Delta\text{-Sr}..\}$ or $\{\Delta\text{-Ca } \nabla\text{-Sr } \Delta\text{-Ca}..\}$ in both OH-channels. Mixed-site substitution such as the ‘12’ configuration is described by combining the site1:site2 descriptors; e.g. $\{1(1), 0(2)\}$ {Ca1} [1,0] [Ca2]. [Fig. 6](#) shows the calculated ‘12’ configuration, displaying only the atoms of interest and revealing the intersite linkage. The data of [Table 4](#) are by no means exhaustive; however, they are sufficient to give a clear picture of site preference versus excess energy.

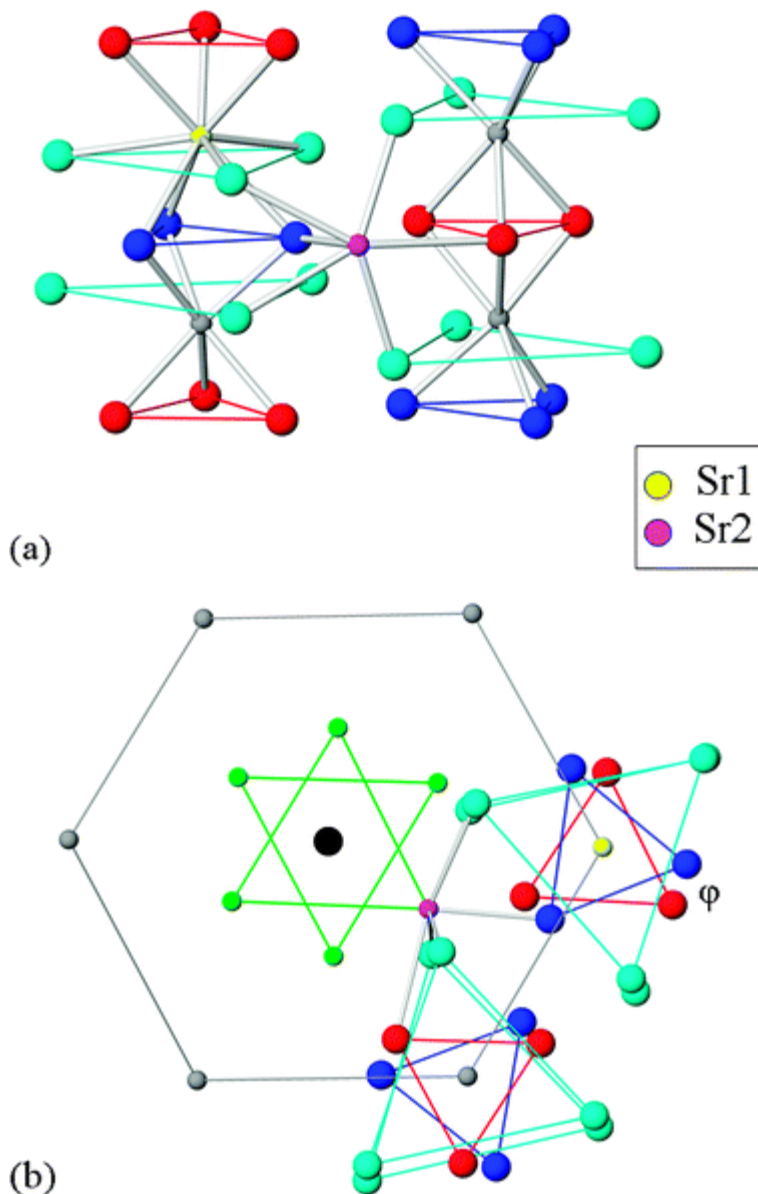


Fig. 6 Top (a) and front (b) view of local cluster obtained from a mixed Sr1, Sr2 configuration (see [Table 4](#)), where Sr at sites 1 and 2 are given as yellow and pink spheres respectively. Atomic color code is otherwise that defined in [Fig. 1](#).

Cation–oxygen bond distances

Pure HA and SrHA. Since the Sr (1.12 Å) ionic radius is larger than that of Ca (0.99 Å), a rigid ion model would suggest a corresponding enlargement of the Sr–O distances in the Sr1O1₃O2₃ and Sr2O1O2O3₄(OH) polyhedra. To check this supposition, consider initially the end members: for pure HA the calculated (experimental, [ref. 24](#)) nearest neighbor Ca1–O1, –O2 bond lengths are 2.40 and 2.43 (2.41, 2.45) Å, respectively, while the three O3 second neighbors are at 2.83 (2.82) Å. For pure SrHA we have obtained (experimental, [ref. 25](#)) 2.54 (2.56) Å for both Sr1–O1, –O2 distances and 2.96 (2.90) Å for Sr1–O3. Turning now to site 2, the calculated (experimental, [ref. 24](#)) Ca2–O distances for pure HA are 2.33 (2.35, 2.37) Å for the near-nearest O3 pair (labeled hereafter as O3*), also bonded to P atoms located at planes above and below the Ca2 plane (see [Fig. 1b](#)). The second pair of O3 atoms, at distances of 2.47 and 2.50 (2.51) Å, are bonded to P atoms positioned in the Ca2 plane. The remaining coordination distances with O2, O_H and O1 are, respectively, 2.34, 2.38 and 2.72 (2.36, 2.39, 2.70) Å.

The corresponding (experimental, [ref. 25](#)) Sr2–O bond lengths for SrHA are –O3* = 2.49, 2.51 (2.51) Å, –O3 = 2.62, 2.68 (2.66) Å, –O2, –OH, –O1 = 2.48, 2.48, 2.74 (2.48, 2.50, 2.76) Å. The excellent agreement between theoretical and experimentally derived bond distances gives confidence in interpretation of the SrHA-X solid solution results.

Site 1 substitution. Let us consider the configurations of [Table 4](#) with Sr at Ca1: analysis of the entire set shows Sr1–O bond lengths falling within the intervals of [2.49, 2.54], [2.54, 2.61] and [2.73, 2.90] Å with ranges of (0.06, 0.08, 0.18) Å for –O1, –O2, –O3, respectively. The Sr1–O1 values are intermediate to those found in HA and SrHA, –O2 distances have expanded relative to either end-member, and both change little with Sr concentration. Meanwhile the –O3 distances lie on a wider interval with all values smaller than those in SrHA. These results show that Sr–O1, –O2 nearest-neighbor bonds are significantly, but weakly affected by the environment, the first contracting, with the second expanding compared to SrHA. The *average* of –O1, –O2 bond lengths is almost independent of Sr concentration. On the other hand, the three second neighbor –O3 display considerable variation, indicating a weaker bond-strength permitting greater distortion of the Sr1–O polyhedron, which will be reflected in twist angles (see below) among other parameters.

Site 2 substitution. The calculated Sr2–O bond distances lie within the intervals [2.39, 2.43], [2.58, 2.68], [2.46, 2.52], [2.46, 2.51] and [2.78, 2.84] Å for Sr2–O3*, –O3, –O2, –OH and –O1, respectively, with the interval sizes ordered as O3*(0.05) < OH (0.06) < O2 = O1 (0.07) < O3 (0.11) Å. It is noticeable that (i) Sr2–O3* bond lengths lie between those obtained for pure HA and SrHA; (ii) values determined for –O3 distances are on the average a bit shorter than those found in SrHA; (iii) –O2 and –OH distances exhibit a small spread around SrHA; (iv) the most distant –O1 shows a notable expansion relative to either end member.

Mixed site 1, site 2 substitution. Analysis of the mixed occupancies confirms the trends seen above for Sr exclusively sited on either Ca1 or Ca2; *i.e.* Sr1–O distances in the mixed cells are inside the intervals of [2.49, 2.54], [2.52, 2.59] and [2.73, 2.91] Å with ranges of (0.06, 0.08, 0.19) Å for –O1, –O2 and –O3 respectively. Sr2–O distances are slightly smaller than those found with Sr purely at Ca2 sites, with ranges –O3* = –OH (0.04) < –O2 (0.05) < –O3 (0.08) < –O1 (0.09) Å.

These results show that Ca1 and Ca2 sites react similarly to Sr incorporation: the nearest oxygen atoms ($R \leq 2.5$ Å) assume bond distances typical of SrHA, while exhibiting a spread in values of 0.05–0.07 Å dependent upon site and local doping conditions. The most salient effects are of Sr1–O2 expansion and Sr2–O3* compression relative to SrHA. The most extended bonds Sr1–O3 (contracted) and Sr2–O1 (expanded) prove to be considerably more flexible, leading to considerable distortion of the Sr–O polyhedra. These results show that Sr1–Sr1, Sr1–Sr2 and Sr2–Sr2 interactions can hardly be distinguished in terms of O–near neighbor bonding within the range of 20 at% Sr content considered, while more distant members of the coordination sphere behave distinctly.

Cation–cation distances

Pure HA and SrHA. As described above, the expansion of 0.31 and 0.38 Å for the cell parameters *a* and *c* between pure HA and SrHA, is accompanied by differential (anisotropic) response of the Sr–O bond lengths. Next we discuss cation–cation distributions as a longer range measure of interactions. The typical 1–1 distances are those between successive cations (*kk*) on a Ca1-column and those sited on adjacent Ca1 columns (Ca1-Y arrangement, [Fig. 1a](#)) belonging to the same plane (*kl:SP*) and different plane (*kl:DP*). The theoretical {*kk*, *kl:SP*, *kl:DP*} values are about [3.44, 5.45, 6.44] and [3.63, 5.63, 6.70] Å for pure HA and SrHA, respectively. The typical 2–2 distances are those between cations lying on a triangle (*e.g.*, Δ) and between ions located in adjacent triangles ($\Delta\nabla$). Ca2- Δ are sandwiched between adjacent ∇ triangles and consequently, have four closer Ca2 neighbors (∇ -c) and two farther neighbors (∇ -f). The calculated [Δ , ∇ -c, ∇ -f] values are [4.09, 4.17, 5.84] and [4.25, 4.38, 6.10] Å for pure HA and SrHA, respectively. Finally, typical 2–1 distances may be defined through the Ca2-V arrangement ([Fig. 1a](#)). They link Ca2 and two successive Ca1 ions on a column *k* sharing coordination of O1 (*k:O1*), and also link Ca2 with two successive Ca1 ions located at the adjacent column *l* sharing coordination with O2 (*l:O2*). The (*k:O1*, *l:O2*) computed values are [3.96, 4.02] and [4.04, 4.22] Å for HA and SrHA

respectively. Typical cation–cation distances presented above are in excellent agreement with those derived from the experimental refinements^{24,25} for end members, suggesting that calculated values for SrHA-X should also be accurate.

Site 1 substitution. We find the range of variation of cation–cation distances for SrHA-X related to site 1: {*kk*, *kl*:SP, *kl*:DP} = [0.19, 0.18, 0.26] Å; the values increase very slightly with Sr content. The distribution is also insensitive to the particular Sr1 arrangement. For example, consider ‘1111’ with configuration {2(0), 2(0)} {Ca1}: here two Ca1 columns are entirely occupied by Sr and two have no Sr content, defining two cation-Y regions and yielding calculated values of [3.48, 5.49, 6.50] Å for adjacent Sr1–Sr1, Sr1–Ca1, and Ca1–Ca1 columns. A very similar set of values is found for a configuration with four Sr evenly distributed throughout the structure.

Site 2 substitution. We find the variation of cation–cation distances for SrHA-X related to site 2: [Δ , ∇ -c, ∇ -f] = [0.14, 0.21, 0.26] Å. There are notable distortions of Ca2 triangles starting from the lowest Sr2 content; *i.e.* one Sr2 in an OH-channel as found in ‘2’, ‘22’, ‘12’, ‘122’ and ‘1222’. We find a shortened Sr2–Ca2 distance of 4.02 Å and lengthened distances of (4.13, 4.15) Å for Sr2–Sr2 and Ca2–Ca2, respectively, for [Δ]. Their average of ~4.09 Å is the value found in pure HA. The Sr2–Ca2 distances related to adjacent triangles [∇ -c, ∇ -f] = [(4.15, 4.25), 5.82] Å; average distances are again close to those of pure HA. OH-channels having two Sr2 at either Δ or ∇ ; *i.e.* one Δ triangle with two Sr2 and its adjacent ∇ triangles with no Sr, present larger and more uniform values for distances inside the occupied triangle and similar distances between adjacent triangles compared to those in OH-channels with one Sr2. Configurations with Sr2 in both triangles ($\Delta\nabla$), continue the trend seen above, indicating that occupancy of adjacent triangles makes distances larger and similar. Examining OH-channels with maximum Sr content confirms that, as the Sr content in $\Delta\nabla$ triangles becomes larger, Sr2–Ca2 distances become closer to those calculated in pure SrHA. However, the Sr2–Sr2 distance is still that of Ca2–Ca2 from pure HA and the distances related to the nearest neighbors between two adjacent triangles lie between those computed for pure end members. Moreover, OH-channels with no Sr substitutions retain Ca2–Ca2 = 4.07 Å inside a Ca2 triangle and distances of 4.21 and 5.89 Å between adjacent triangles.

Mixed site 1, site 2 substitution. Investigation of site 1 using mixed configurations yields data for Sr1-Y and Ca1-Y columns, similar to those of pure site 1 substitutions. However, Sr1-Y [*kl*:SP, *kl*:DP] values span a larger range compared to pure Sr1 configurations and more narrow intervals associated with Ca1-Y columns. Detailed examination of the data suggests that the Sr1 site is progressively more geometrically distorted in the presence of increasing Sr2 concentration. These effects are not large, since both average and range of typical values are comparable to those derived from the ‘11’ composition. We have also calculated lesser variations of [0.08, 0.20] Å for the site 1, site 2 (*k*:O1, *l*:O2) set; as these configurations involve no aligned ions, this range is surprisingly small.

In summary, we find comparable variation for typical cation–cation distances whenever multiple substituents are aligned parallel with *a* and *c* directions; *e.g.* 1–1 and 2–2 distances labeled as {*kk*, *kl*:SP} and [Δ], respectively. Larger values are found whenever such alignment is missing, since in this case, cation–cation distances incorporate expansions of both ‘local’ *a* and *c* cell parameters. The variation of cation–cation distances is very different from a uniform expansion with Sr content, as seen in XRD average cell and site parameters. Site1-related distances are rather insensitive to Sr content, while Site2 distances are highly anisotropic and vary notably with concentration. The near equivalence of Ca2–Ca2 and Sr2–Sr2 distances is a surprising result, with consequences for attempts to model the interatomic potentials needed for a full phase-diagram study.

Twist angle

Along with cell parameters, the Ca1O1₃O2₃ metaprismatic twist angle (φ) has been proposed^{29–31} as a useful tool for characterizing and comparing apatite compounds. This angle is defined as the O1–Ca1–O2 twist angle projected onto (001) plane of the Ca1O1₃O2₃ metaprism (see Fig. 1a). Dong and White^{29,31} calculated φ for a range of apatites and observed an inverse linear relationship with the ionic radius of the Ca1 site and the ‘average crystal ionic radius’. Thus, since the ionic radius of Sr is greater than Ca, pure SrHA must present an enlargement of Sr1–O and Sr2–Sr2 distances and both structural modifications can be achieved by reducing φ . We have calculated $\varphi = 23.02^\circ$ and 22.76° for pure HA

and SrHA, respectively, which are close to experimentally derived values of 23.13° and 22.97° .^{24,25} Due to its high sensitivity to cation size and the successful empirical parameterization, we have investigated φ as a characteristic of the Sr environment in all configurations of [Table 4](#). Needless to say, in the distorted and disordered SrHA-X environment, a variety of values of φ are realized, and only some average value may be compared to experimental data. Further, since φ is related directly to site 1, distortions about site 2 are not ‘encoded’. Here we take into consideration twist angles related to the central cation of Y- and the cation-columns of V-arrangements to analyze the structural impact of Sr.

Ca1-Y Arrangements. We have eleven different Y-arrangements in site 1; to make the discussion clear, the notation is extended to include information about the three cation types (Ca1, Sr1) around the central cation, and whether the cations are on mixed (m) or pure (p) columns. In pure HA only one Y-arrangement is found, as represented by Ca1p-Y(Ca1p); *i.e.* central Ca1 on a pure Ca1-column is surrounded by three Ca1 which in turn are sited on pure Ca1-columns. Such an arrangement is present in ‘1’, ‘12’, ‘112’, ‘122’ and ‘1222’ configurations as well. The twist angle associated is $\sim 23.01^\circ$ and increases with the Sr content in adjacent columns. Thus we have calculated $\varphi = 23.53, 24.40$ and 24.51° for Ca1p-Y(Ca1m,Ca1p,Ca1p), $-Y(\text{Ca1m,Ca1m,Ca1p})$ and $-Y(\text{Sr1p,Ca1p,Ca1p})$, respectively. Analyses of Sr1-Y confirm the trend: considering first Sr1m-Y arrangements, we have computed twist angles $24.79, 25.91, 26.78$ and 27.52° for the Sr1m-Y(Ca1p), $-Y(\text{Sr1m,Sr1m,Ca1p})$, $-Y(\text{Sr1m})$ and $-Y(\text{Sr1p,Sr1p,Ca1p})$, respectively. Note that Y-arrangements of mixed composition cited above have no Sr2 occupancy. Finally the Sr1p-Y arrangements yield $\varphi = 25.80, 27.14$ and 28.55° for Sr1p-Y(Ca1p), $-Y(\text{Sr1m,Sr1m,Ca1p})$ and $-Y(\text{Sr1p,Sr1p,Ca1p})$, respectively. These results are interesting and unexpected because both Sr1–O distances and twist angles are increasing with Sr-content. The latter Sr1p-Y(Sr1p,Sr1p,Ca1p) arrangement is particularly surprising since its twist angle is 5.79° larger than that associated with pure SrHA which has only the Sr1p-Y(Sr1p) arrangement. Thus the Sr1 occupancies may generate twist angles even larger than the pure end member.

Ca2-V arrangements. Next consider Ca2-V arrangements: taking pure HA as an example we have Ca2-V(O1–Ca1p,O2–Ca1p), where O1 and O2 are coordinated to Ca2, and Ca1p represents the two pure Ca1-columns on which the O1 and O2 triangles are centered. We are dealing with two twist angles (φ_1, φ_2) since two Ca1 columns are involved. We have examined the diverse Ca2-V arrangements available in 211 supercells; *e.g.* OH-channels with one Sr at one Δ triangle yields Sr2-V(O1–Ca1p,O2–Ca1p) arrangements found in ‘2,’ ‘22’, ‘222’ and ‘122’ configurations. The values of (φ_1, φ_2) for single Sr2-V lie inside the intervals $\varphi_1 = [19.04, 23.00^\circ]$ and $\varphi_2 = [20.51, 23.11^\circ]$. For the highest Sr content ‘2222’ and ‘2222a’ we calculate the intervals of $\varphi_1 = [18.50, 19.74^\circ]$ and $\varphi_2 = [18.50, 23.23^\circ]$. Finally, we considered mixed compositions with one Sr at Δ as found in OH-channels in ‘12’ and ‘122’. Analysis of all Ca2-V arrangements shows that twist angles fall between those found in pure HA and SrHA for low Sr content and are smaller than in pure SrHA for higher Sr content. Sr2 occupancy generates a smaller twist angle in both columns associated with the Ca2-V arrangement, $\varphi_1 < \varphi_2$ in all cases. Thus the Ca2-V arrangement acts inversely to the twist angle as compared to Ca1–Y

In summary, Ca1-Y arrangements with Sr1 occupancy display increasing twist angles φ , which can exceed that of pure SrHa. If we consider that (i) increasing φ tends to minimize the O–O repulsion on the metaprism (see [Fig. 6](#)), and (ii) near-neighbor Sr1–O distances are comparable to those of pure SrHA, this can be considered a stabilizing mechanism. The lower values found for φ (\leq pure SrHA) in Ca2-V arrangements thus suggest a less stable Sr2 site.

Excess energies

The excess energies E_x of the solid solution SrHA-X structures studied relative to those of the two end members HA and SrHA are listed in [Table 4](#) and shown graphically in [Fig. 7](#). E_x is defined in terms of the energy per unit cell of each structure as $E_x = E(\text{Sr}_x\text{Ca}_{1-x}\text{HA}) - xE(\text{SrHA}) - (1 - x)E(\text{HA})$, where x runs between 0 and 1, and lattice energies are normalized per cation site. It is observed that E_x presents positive values for all compositions, which suggests that these compositions are unstable relative to the corresponding end members HA and SrHA at 0 K. At finite temperature the entropy of mixing provides a stabilizing free energy term $-T\Delta S$. Within each specific Sr occupancy, E_x is seen to be ordered as $E_x(\text{site}$

1) $< E_x(\text{mixed sites}) < E_x(\text{site 2})$, indicating that Sr incorporation at site 1 is energetically more favorable than at mixed sites followed by site 2. It is noticed that E_x varies linearly with Sr content in mixed and site 2 occupancies with very similar slopes, while a decreased slope is obtained for site 1 compositions; *i.e.* it costs relatively more to add one more Sr2. In other words, Sr1–Sr1 repulsion is less than Sr1–Sr2 \approx Sr2–Sr2. Comparison of E_x values between $\text{Sr}_x\text{Ca}_{1-x}\text{HA}$ and $\text{Pb}_x\text{Ca}_{1-x}\text{HA}$ solid solutions³² shows that Sr substitution for Ca causes less stress on the HA structure than Pb incorporation. This result is unexpected considering a rigid ion model, since Pb^{2+} and Sr^{2+} have similar ionic radii. Pb substitution for Ca2, both experimentally and theoretically, is found to be always preferred, while Sr is predicted to prefer the Ca1 site (at 0K) for all concentrations studied. Experimentally the Rietveld XRD refinement (Table 3) shows a preferential substitution of Sr for Ca1 at 1% concentration, a random substitution at 5% and a slight preferential occupancy for the Ca2 site at 10 and 15% Sr content.

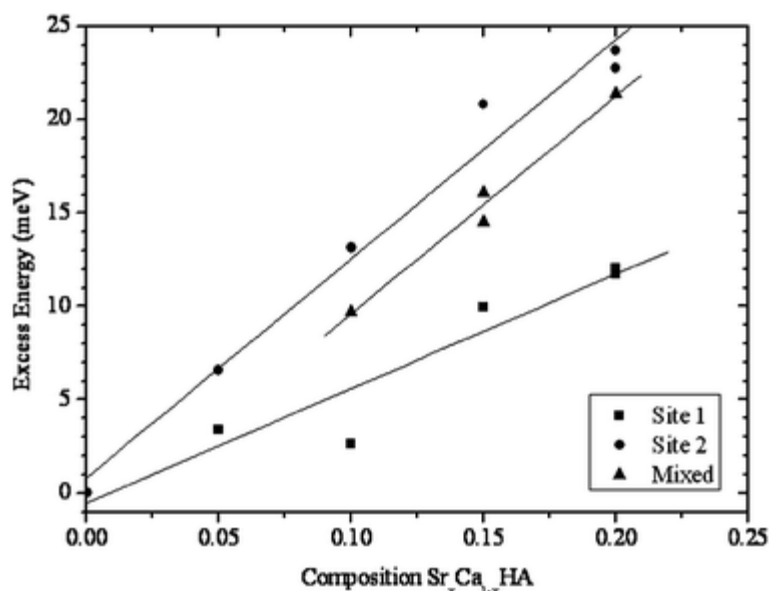


Fig. 7 Excess energy E_x per cation site *versus* Sr composition and neighbor configuration as given in Table 4.

At this point, it is desirable to establish chemical and/or structural arguments for the clearly predicted energetic preference for Sr1 in SrHA-X. As discussed above, the nearest neighbors Sr1–O and Sr2–O bond structures are comparable to SrHA. The longer Sr–O bonds show greater flexibility, and contribute to a marked distortion of the metal-oxygen polyhedron, one measure of which is the twist angle studied here, following literature practice. Typical cation–cation distances suggest that Sr induces more distortion at site 2 than site 1; this distortion may be responsible for the higher energy of site 2. As seen in Fig. 7, values and slope of E_x *versus* Sr content for both mixed and site 2 occupancies are similar, and quite different from those obtained for site 1. This indicates that the cation–cation repulsion associated with site 2 is more influential in raising energy than the O–O repulsion related to site 1, which is minimized by increasing twist angle. Furthermore, the reversal of site preference for Pb (both in experiment and theory) suggests that details of quantum chemical bonding may be of greater importance.

5. Conclusions

Wet synthesis methods have been employed to produce Sr-doped nanocrystalline hydroxyapatite, with up to 15 at.% Sr. X-Ray fluorescence, Rietveld refinement of XRD data, analysis of IR vibrational bands associated with OH and phosphate groups, and EXAFS modeling of the Sr K-edge region permit a near-atomic level analysis of Sr-induced structural modification. The EXAFS model Sr–O distance is compatible with either site Ca1 or site Ca2. Rietveld analysis shows a preference for Sr1 occupancy at ~1 at.% concentration; by 5% the Sr2/Sr1 ratio is that expected on a statistical basis, and grows progressively

with Sr content. This is contrast to the well-studied case of Pb^{+2} where a marked preference for site 2 is seen, and in disagreement with previous studies on large crystals formed by solid state diffusion⁴ and by wet synthesis⁸ for concentrations >10 at.% Sr. Since Sr^{+2} and Pb^{+2} have similar ionic radii, previously used ionic-size arguments for site preference are questionable; therefore, first principles DFT band-structure calculations were carried out, in which ionic positions were fully relaxed for a considerable number of Sr-substituted configurations. Resulting excess energy values confirm the preference for site 1 at 0 K; however, the energy differences are rather small. Detailed analyses of cation–oxygen bond distributions, cation–cation distances, and site1–oxygen polyhedron twist angles were made in order to provide an atomic-scale interpretation of the observed structural modifications. The cation–oxygen near-neighbor environment does not permit significant discrimination between Sr1 and Sr2. Analysis of cation–cation distances suggests that Sr induces more distortion at site 2 than site 1, and this may be related to the higher energy of site 2. Sr2 occupancy generates a smaller twist angle in both Ca-columns associated with Ca2-V; such reduction increases Ca1 metaprism O–O repulsion, which may be an additional factor in raising the Sr2 excess energy. Supercell sampling of a considerable number of Sr-substituted configurations accounts for some of the features of disorder (bond length variations, angular distortions) seen in IR spectra and EXAFS. Investigation of effects of OH loss, also seen, should be considered in future studies.

Acknowledgements

This work was supported by the Chemical Sciences, Geosciences and Biosciences Division, Office of Basic Energy Sciences, Office of Sciences, U.S. Department of Energy, Grant No. DE-FG-02-03ER15457. and by CNPq, Brazil. X-Ray diffraction was carried out at the ID15B Beamline of the European Synchrotron Radiation Facility (ESRF).

References

- 1 G. Stylios, T. Wan and P. Giannoudis, *Injury Int. Care Injured*, 2007, **38S1**, S63–S64.
- 2 M. Vallet-Regi and J. M. González-Calbet, *Progress in Solid State Chemistry*, 2004, **32**, 1–31.
- 3 L. L. Hench and J. R. Jones, in *Biomaterials, artificial organs and tissue engineering*, ed. L. L. Hench and J. R. Jones, Woodhead Publishing Limited, 2005.
- 4 A. Bigi, M. Falini, M. Gazzano and N. Roveri, *Mater. Sci. Forum*, 1988, **814**, 278–281.
- 5 S. C. Verberckmoes, G. J. Behets, L. Oste, A. R. Bervoets, L. V. Lamberts, M. Drakopoulos, A. Somogyi, P. Cool, W. Dorrine, M. E. De Broe and P. C. D'Haese, *Calcif. Tissue Int.*, 2004, **75**, 405–415 [[Links](#)].
- 6 W. Chen, Z. L. Huang, Y. Liu and Q. J. He, *Catal. Commun.*, 2008, **9**, 516–521 [[Links](#)].
- 7 A. Bigi, E. Boanini, C. Capuccini and M. Gazzano, *Inorganica Chimica Acta*, 2007, **360**, 1009–1016.
- 8 S. G. Dahl, P. Allain, P. J. Marie, Y. Mauras, G. Boivin, P. Ammann, Y. Tsouderos, P. D. Delmas and C. Christiansen, *Bone*, 2001, **28**, 446–453 [[Links](#)].
- 9 J. Christoffersen, M. R. Christoffersen, N. Kolthoff and O. Barenholdt, *Bone*, 1997, **20**, 47–54 [[Links](#)].
- 10 E. Landi, S. Sprio, M. Sandri, G. Celotti and A. Tampieri, *Acta Biomater.*, 2007, DOI:[10.1016/j.actbio.2007.10.010](https://doi.org/10.1016/j.actbio.2007.10.010).
- 11 E. Landi, A. Tampieri, G. Celotti, S. Sprio, M. Sandri and G. Logroscino, *Acta Biomater.*, 2007, **3**, 961–969 [[Links](#)].
- 12 G. X. Ni, W. W. Lu, B. Xu, K. Y. Chiu, C. Yang, Z. Y. Li, W. M. Lam and K. D. K. Luk, *Biomaterials*, 2006, **27**, 5127–5133 [[Links](#)].
- 13 D. Guo, K. W. Xu, X. Y. Zhao and Y. Han, *Biomaterials*, 2005, **26**, 4073–4083 [[Links](#)].
- 14 K. Zhu, K. Yanagisawa, R. Shimanouchi, A. Onda and K. Kajiyoshi, *Journal of the European Ceramic Society*, 2006, **26**, 509–513.
- 15 A. Nounah, J. Szilagyi and J. L. Lacout, *Ann. Chim France*, 1990, **15**, 409–419.
- 16 *MATLAB*: The Mathworks Inc. <http://www.mathworks.com>.
- 17 R. A. Young, in *The Rietveld method*, ed. R. A. Young, International Union of Crystallography, Oxford

- University Press, Oxford, 1995; H. M. Rietveld, *Acta Crystallogr.*, 1967, **22**, 151–152 [\[Links\]](#).
- 18 J. Rodriguez-Carvajal, in *An introduction to the program FullProf version 2001*, Laboratoire Léon Brillouin, CEA-CNRS, Saclay, France, 2001.
- 19 J. J. Rehr, J. De Leon Mustre, S. I. Zabinski and R. C. Albers, *J. Am. Chem. Soc.*, 1991, **113**, 5135–5140 [\[Links\]](#).
- 20 M. Newville, B. Ravel, D. Haskel, J. J. Rehr, A. Stern and Y. Yacoby, *Physica*, 1995, **B208&209**, 154–156.
- 21 G. Kresse and J. Hafner, *Phys. Rev.*, 1993, **B47**, 558–561.
- 22 G. Kresse and J. Furthmüller, *Phys. Rev.*, 1996, **B54**, 11169–11186.
- 23 G. Kresse and J. Furthmüller, *Comput. Mater. Sci.*, 1996, **6**, 15–50 [\[Links\]](#).
- 24 M. I. Kay, R. A. Young and A. S. Posner, *Nature*, 1964, **204**, 1050–1052 [\[Links\]](#).
- 25 K. Sudarsanan and R. A. Young, *Acta Crystallogr., Sect. B: Struct. Crystallogr. Cryst. Chem.*, 1972, **28**, 3668–3670 [\[Links\]](#).
- 26 G. Engel and W. E. Klee, *J. Inorg. Nucl. Chem.*, 1970, **32**, 1837–1843 [\[Links\]](#).
- 27 B. O. Fowler, *Inorg. Chem.*, 1974, **13**, 194–207 [\[Links\]](#).
- 28 J. E. Harries, D. W. L. Hukins and S. S. Hasnain, *J. Phys. C: Solid State Phys.*, 1986, **19**, 6859–6872 [\[Links\]](#).
- 29 T. J. White and Z. L. Dong, *Acta Crystallogr., Sect. B: Struct. Sci.*, 2003, **59**, 1–16 [\[Links\]](#).
- 30 P. H. J. Mercier, Y. Le Page, P. S. Whitfield, L. D. Mitchell and T. J. White, *Acta Crystallogr., Sect. B: Struct. Sci.*, 2005, **61**, 635–655 [\[Links\]](#).
- 31 (a) Z. L. Dong and T. J. White, *Acta Crystallogr., Sect. B: Struct. Sci.*, 2004, **60**, 138–145 [\[Links\]](#);
(b) Z. L. Dong and T. J. White, *Acta Crystallogr., Sect. B: Struct. Sci.*, 2004, **60**, 146–154 [\[Links\]](#).
- 32 D. E. Ellis, J. Terra, O. Warschkow, M. Jiang, G. B. González, J. Okasinski, M. J. Bedzyk, A. M. Rossi and J. G. Eon, *Phys. Chem. Chem. Phys.*, 2006, **8**, 967–976 [\[Links\]](#).

Footnote

† Electronic supplementary information (ESI) available: Powder diffraction cif files for Sr1B2, Sr5B2, Sr10B2 and Sr15B2. See DOI: [10.1039/b802841a](https://doi.org/10.1039/b802841a)

This journal is © the Owner Societies 2008